Sensors & Diagnostics

PAPER

View Article Online
View Journal

Cite this: DOI: 10.1039/d6sd00020g

A novel label-free EC aptasensor for early detection of H9N2 influenza using FFT-square wave voltammetry and validated by molecular docking

Negar Heidari,[ab] Nogol D. Moghaddam,[b] Sharmin Kharrazi,[c] Jahan B. Ghasemi,[b] Melika F. Aghdam,[b] Mahdi Amrollahi Bioyki,[a] Ebrahim Ghafar-Zadeh *[a] and Parviz Norouzi*[ab]

H9N2 avian influenza threatens global poultry production and human health through cross-species transmission and its role as a genetic reservoir for emerging influenza strains, underscoring the need for rapid and reliable early detection. Here, we report a label-free electrochemical aptasensor based on the B4 anti-H9N2 hemagglutinin (HA) aptamer, implemented for the first time as a biorecognition element in an electrochemical sensing platform. Compared to conventional antibody-based systems, the B4 aptamer offers high binding affinity, improved structural stability, and the ability to recognize intact viral particles, enabling reliable label-free detection. Computational modeling, including molecular docking and molecular dynamics (MD) simulations, was employed to evaluate aptamer–target interactions and to screen candidate sequences against structurally related viral targets, achieving predicted specificity of approximately 90–95%. This approach supports rational aptamer selection and reduces experimental trial-and-error. The sensing interface integrates cerium oxide nanoparticles (CeO_2), electrochemically reduced graphene oxide (rGO), and electrodeposited gold nanoparticles (AuNPs) to form a conductive and stable nanostructured platform. A PolyA–PolyT-modified aptamer enables thiol-free, orientation-controlled immobilization *via* adenine–gold affinity, improving target accessibility and reducing steric hindrance, while CeO_2 enhances biomolecule adsorption and immobilization stability. Signal transduction was performed using fast Fourier transform square-wave voltammetry (FFT-SWV) within a simplified, miniaturized potentiostat architecture, where part of the signal filtering is transferred from hardware to software. This approach suppresses capacitive background and noise in the frequency domain, improving signal-to-noise ratio and enabling lower detection limits while supporting portable implementation. Under optimized conditions, the aptasensor exhibited a linear response over 1.0×10^1 to 1.0×10^5 PFU mL^{-1} with a detection limit of 0.25 PFU mL^{-1} ($R^2 \approx 0.99$). The sensor demonstrated high selectivity, excellent reproducibility (RSD $< 4\%$), and stable performance over ten days, with retained performance in allantoic fluid, confirming robustness in complex biological matrices. This work presents a sensitive and modular electrochemical sensing platform that integrates computationally guided aptamer design, engineered nanointerfaces, and advanced signal processing, offering strong potential for portable and point-of-care viral detection.

Received 18th February 2026,
Accepted 29th April 2026

DOI: 10.1039/d6sd00020g

rsc.li/sensors

1. Introduction

H9N2 avian influenza virus (AIV) is one of the most widespread low-pathogenic influenza subtypes, responsible for chronic losses in poultry production across Asia, the Middle East, and Africa.[1] Although infections in birds are often mild, co-infection with other pathogens leads to high mortality and severe economic damage.[2–4] More critically, H9N2 can infect humans and swine and acts as a genetic reservoir for the generation of reassortant influenza strains with pandemic potential. This dual threat—economic and zoonotic—makes rapid and reliable early detection essential for both veterinary and public-health surveillance.[2,5,6]

Current diagnostic assays for avian influenza, such as polymerase chain reaction (PCR) and enzyme-linked

[a] Dept. of Electrical Engineering and Computer Science, Lassonde School of Engineering, York University, Toronto, Canada. E-mail: egz@yorku.ca, pnorouzi@yorku.ca
[b] School of Chemistry, College of Science, University of Tehran, P.O. Box 14155-6455, Tehran, Iran
[c] Department of Medical Nanotechnology, School of Advanced Technologies in Medicine, Tehran University of Medical Sciences, Tehran, Iran

immunosorbent assay (ELISA), provide high sensitivity and specificity but are constrained by complex sample preparation, expensive reagents, and the need for trained personnel and laboratory infrastructure.[7,8] Other label-free approaches, including Raman spectroscopy, quartz crystal microbalance (QCM), and surface plasmon resonance (SPR), offer direct detection of viral proteins but remain dependent on sophisticated instrumentation and are unsuitable for rapid, on-site screening.[9,10] These limitations highlight the necessity for portable, low-cost, and user-friendly biosensing technologies capable of providing early viral detection in resource-limited environments.[11]

In this context, electrochemical (EC) biosensors provide rapid, sensitive, and miniaturization-ready pathogen detection through label-free monitoring of interfacial electron-transfer processes.[12] While many avian influenza EC sensors rely on antibodies, their cost, thermal fragility, and batch variability can limit portability and reproducibility.[13–17] Aptamers, selected by SELEX, offer a stable and easily modifiable alternative suited for controlled immobilization on electrode surfaces, making aptamer-based EC platforms well suited for detecting viral antigens such as the H9N2 hemagglutinin (HA) protein.[18,19] For H9N2, the DNA aptamer B4 was first reported by Zhang *et al.*[20] following capillary electrophoresis SELEX (CE-SELEX) against purified hemagglutinin (HA). B4 (~70 nt) showed low-nanomolar binding affinity to H9N2 HA and was also experimentally confirmed to bind intact H9N2 virions with comparable affinity, indicating recognition of an HA epitope accessible on the native virus surface.[20] This affinity was supported by orthogonal validations including CE mobility shift, ELAA binding curves, and fluorescence microscopy imaging of virus-bound aptamer.[20] However, despite this prior validation, B4 has not been translated into a biosensor format as a biorecognition element for analytical virus detection (electrochemical or otherwise), leaving a gap between established molecular recognition and deployable sensing. Leveraging this high-affinity aptamer, with its strong and consistent interaction with hemagglutinin, therefore represents a novel opportunity to develop a selective, stable, and reproducible alternative to conventional antibody-based recognition strategies.

Electrode fouling and aptamer aggregation remain major obstacles in label-free electrochemical aptasensors. Incorporation of conductive nanomaterials provides an effective means to overcome these issues. Electrochemically reduced graphene oxide (rGO) offers high conductivity and large surface area for efficient electron transfer and stable aptamer immobilization, while cerium oxide nanoparticles (CeO_2 NPs) prevent rGO restacking through oxygen-vacancy-mediated interactions that enhance charge transfer and interfacial stability.[21,22] The resulting CeO_2–rGO composite forms a robust, biocompatible matrix that, when decorated with gold nanoparticles (AuNPs), not only accelerates electron-exchange kinetics but also provides adenine-binding sites for oriented, thiol-free aptamer attachment with reduced nonspecific adsorption. Coupling this hierarchical nanocomposite with fast Fourier transform square-wave voltammetry (FFT-SWV), which converts time-domain electrochemical signals into the frequency domain to isolate Faradaic responses and suppress background noise, markedly improves signal-to-noise ratio, sensitivity, and analytical reproducibility.[23]

This study presents the first electrochemical aptasensor for the specific and sensitive detection of the H9N2 avian influenza virus using the B4 aptamer as a high-affinity biorecognition element. Previously identified through SELEX for strong binding to hemagglutinin (HA), the B4 aptamer provides a stable and reproducible alternative to conventional antibody-based recognition and is capable of interacting with intact viral particles. Molecular docking, together with molecular dynamics (MD) simulations, further supports its selective interaction with HA at the residue level and enables evaluation of binding stability and specificity against structurally related viral targets, thereby facilitating rational selection of a robust recognition element. The sensing platform integrates a nanostructured rGO/CeO_2/AuNP composite, enabling conductive and stable immobilization of a PolyA–PolyT-modified aptamer with improved orientation and target accessibility compared to conventional approaches. The successful fabrication and interfacial integrity were confirmed using standard electrochemical and morphological characterization techniques (CV, EIS, and FE-SEM).Signal transduction was performed using fast Fourier transform square-wave voltammetry (FFT-SWV), which enhances sensitivity by selectively extracting Faradaic responses while suppressing capacitive background signals, particularly in complex biological environments such as allantoic fluid. The aptasensor achieved a detection limit of 0.25 PFU mL^{-1}, demonstrating a sensitive and adaptable platform with strong potential for viral detection and future point-of-care applications.

2. Materials and methods

2.1 Materials and reagents

Gold(III) chloride hydrate ($HAuCl_4 \cdot 4H_2O$, 99%), graphene oxide (GO, 99%), cerium oxide nanopowder (CeO_2, <25 nm), potassium ferrocyanide ($K_4[Fe(CN)_6]$), potassium ferricyanide ($K_3[Fe(CN)_6]$), and potassium chloride (KCl) were procured from Sigma-Aldrich. All remaining chemicals were of analytical grade and used as received without further purification. Phosphate-buffered saline (PBS, 10 mM Na_2HPO_4, 10 mM KH_2PO_4, 150 mM NaCl, pH 7.5) and PBST buffer (10 mM Na_2HPO_4, 10 mM KH_2PO_4, 0.05% [w/v] Tween 20, pH 7.5) were freshly prepared with Milli-Q deionized water.

2.1.1 Aptamer and viruses. The DNA aptamer B4 targeting the H9N2 hemagglutinin (HA) protein was selected based on the sequence reported by Zhang *et al.*[20] (5′-GGG CCG CGC CTG GTC GGT TGG GTG GGT GGC GCC CGG GAC GTT TTT AAA AAA AAA A-3′). This oligonucleotide was ordered and

synthesized by SinaClon Biotechnology Company (Tehran, Iran) following the synthesis and purification approach described in Zhang *et al.*[20] The 3′-terminal tail (T5–A10) provides thymine spacing and an adenine-rich segment that promotes stable, high-density immobilization on the AuNP-modified surface *via* adenine–gold affinity, facilitating a more accessible and orientation-favored configuration of the aptamer compared to random adsorption.[24–27] The aptamer–HA interaction was further evaluated in this work by molecular docking, which supported favorable binding between B4 and the HA target. The H9N2 AIV (A/Chicken/Iran/99/H9N2) at a concentration of 1.0×10^8 PFU mL^{-1} in an allantoic fluid environment and pure allantoic fluid were provided by Razi Vaccine & Serum Research Institute, Shiraz, Iran. A lyophilized powder of inactivated avian influenza virus subtype H5N8 was obtained and used as a non-target analyte for selectivity evaluation. The viral powder was reconstituted in DNase/RNase-Free DI and gently vortexed until fully dissolved. A quadrivalent inactivated influenza vaccine, VaxigripTetra®, was also obtained from Sanofi S.A. (France) and used as a non-target analyte for selectivity evaluation. The H5N8 sample and the vaccine were stored at 2–8 °C and used without further purification.[28] The aptamer was reconstituted in DNase/RNase-Free DI to a final stock concentration of 100 μM and stored at −20 °C until use, with aliquots for routine experiments stored at 4 °C. The H9N2 and pure allantoic fluid were stored at −20 °C until use, with aliquots for frequent experiments stored at 4 °C, and dilutions of the two fluids were conducted with DNase/RNase-Free DI.

2.2 Apparatus

All pH measurements were made with a pH meter (MP512 precision pH meter, Shanghai San-Xin Instrumentation). All sonication steps were performed in an ultrasound bath (B8510, Branson Ultrasonics Corporation). Surface morphology and elemental composition of the samples were analyzed using a field emission scanning electron microscope (FE-SEM, TESCAN MAIA3) equipped with an EDX detector. SEM images and EDX spectra were obtained under appropriate accelerating voltages depending on the sample type.

2.2.1 EC measurements. A conventional three-electrode system, including a gold electrode (2 mm in diameter) as the working electrode, an Ag/AgCl electrode as the reference electrode, and a platinum wire as the counter electrode, was used in all experimental steps, with all potentials referred to the reference electrode. Electrochemical experiments involving cyclic voltammetry (CV) and electrochemical impedance spectroscopy (EIS) were performed using a PalmSens potentiostat device (Palm Instrument BV, the Netherlands/PalmSense4, the Netherlands), with data acquisition and analysis conducted using the PS-Trace 5.9 softwareAll FFT-SW voltammetric measurements were carried out using a homemade potentiostat developed for this study (see SI, section S1). A software application developed in Delphi 6.0 was utilized to apply the excitation waveform and to acquire, analyze, and store the obtained current data. In this system, part of the conventional analog filtering and signal-conditioning stages is replaced by FFT-based digital signal processing, enabling effective separation of Faradaic signals from background noise and improving the signal-to-noise ratio. This approach allows simplification of the electronic circuitry and provides a pathway toward miniaturized, portable implementations. The same algorithmic framework is readily transferable to modern mobile platforms (iOS and Android), enabling real-time data processing and wireless communication (*e.g.*, *via* WiFi) for on-site monitoring. The applied waveform contains multiple SW cycles with an amplitude of E_{sw} and frequency of f_0, superimposed on a staircase potential function, and changed by a small potential step of ΔE.

2.3 Fabrication of modified Au electrode and aptasensor

The preparation procedure for Au/nanoCeO_2–rGO/AuNPs was as follows. Firstly, a 1 mg mL^{-1} GO dispersion was obtained by adding 1 mg of GO powder to 1 mL of deionized water and subjecting it to ultrasound bath irradiation for 2 hours.[29] Then, 1 mg of nanoCeO_2 powder was added to 1 mL of the obtained GO dispersion and sonicated for an additional 90 minutes. This resulted in a homogeneous nanoCeO_2–GO (1 : 1 W/W) composite.[23] The gold electrode surface was cleaned through two steps. Initially, it was mechanically polished using α-alumina slurry (0.3 μM in diameter). After rinsing, the electrode was immersed in a 0.5 mol L^{-1} H_2SO_4 solution and cycled in the potential range of −0.3 to 1.6 V at a scan rate of 0.1 V s^{-1} for 40 scans. The pristine gold electrode surface was thoroughly cleaned with deionized water and dried under an infrared (IR) lamp. Subsequently, 6 μL of nanoCeO_2–GO was pipetted onto the clean electrode surface and dried using an IR lamp. Following this, electro-deposition of AuNPs was conducted *via* the chronoamperometry method under a constant potential of −0.9 V in a 0.1 mol L^{-1} PBS solution, pH 6.5, containing 1 mmol L^{-1} $HAuCl_4{\cdot}3H_2O$ for 250 seconds.[29,30] During this co-reduction, the present GO layers on the electrode surface were electrochemically reduced to rGO, and a thin layer of AuNPs was electrodeposited on the electrode surface. The prepared electrode was then washed with DI water.

2.3.1 Aptamer immobilization and H9N2 detection. A drop of 10 μL of the 5 μM diluted aptamer in PBS, pH 7.5, was immobilized on Au/nanoCeO_2–rGO/AuNPs electrode, which was then incubated for 8 h at −4 °C (Au/nanoCeO_2–rGO/AuNP/aptamer). Then, the aptasensor was subjected to an appropriate concentration of 10 μL of H9N2 for 90 min at room temperature and named as Au/nanoCeO_2–rGO/AuNP/

aptamer/H9N2. The construction steps of the aptasensor and measurements are illustrated in Scheme 1.

2.4 Molecular docking

Molecular docking studies were conducted using the HDOCK server (http://hdock.phys.hust.edu.cn), which provides a hybrid docking algorithm optimized for protein–nucleic acid interactions.[31] From the HDOCK results, key docking parameters such as docking score, ligand RMSD, confidence score, and interface residues were extracted for each aptamer–protein complex. The crystal structure of the target viral protein (PDB ID: 1JSD) was obtained from the Protein Data Bank. Structural preparation of the receptor, including addition of polar hydrogen atoms, and energy minimization, was performed using BIOVIA Discovery Studio 2016 (version 4.1). Missing side chains, if any, were also modeled during this step. The aptamer structures, including the primary aptamer B4 and nine additional candidate sequences, were generated in three-dimensional format and converted to PDB files suitable for docking. Each aptamer was docked individually to the viral protein in global docking mode, where no prior knowledge of the binding site was required. HDOCK automatically recognized the receptor as a protein and the ligand as a DNA strand. To ensure reproducibility and capture conformational variability, ten independent docking runs were performed per aptamer. From each run, the top-ranked pose (model 1) was extracted. The final docking score reported for each aptamer represents the average of these ten top poses, while the final docking visualization of B4 was based on the pose with the best docking score among ten independent runs.

For each selected complex, the docking score (in kcal mol^{-1}), confidence score, ligand RMSD, and interfacial residues involved in binding were recorded. Interatomic contacts between receptor and ligand were identified based on interatomic distances ranging from 1.4 to 5.0 Å, as commonly employed in docking interaction analysis[32] and categorized by their electrostatic or polar nature. Interface residues and docking poses were visualized and analyzed using BIOVIA Discovery Studio 2016 (v4.1). Additionally, the orientation of B4 aptamer was assessed to determine whether its 3′-end remained accessible for electrode immobilization while allowing the 5′-end to participate in target binding.

3. Result and discussion

3.1 Structural and morphological characterization

3.1.1 FE-SEM and EDX elemental composition and map. FE-SEM imaging (Fig. 1a–d) captures the stepwise evolution

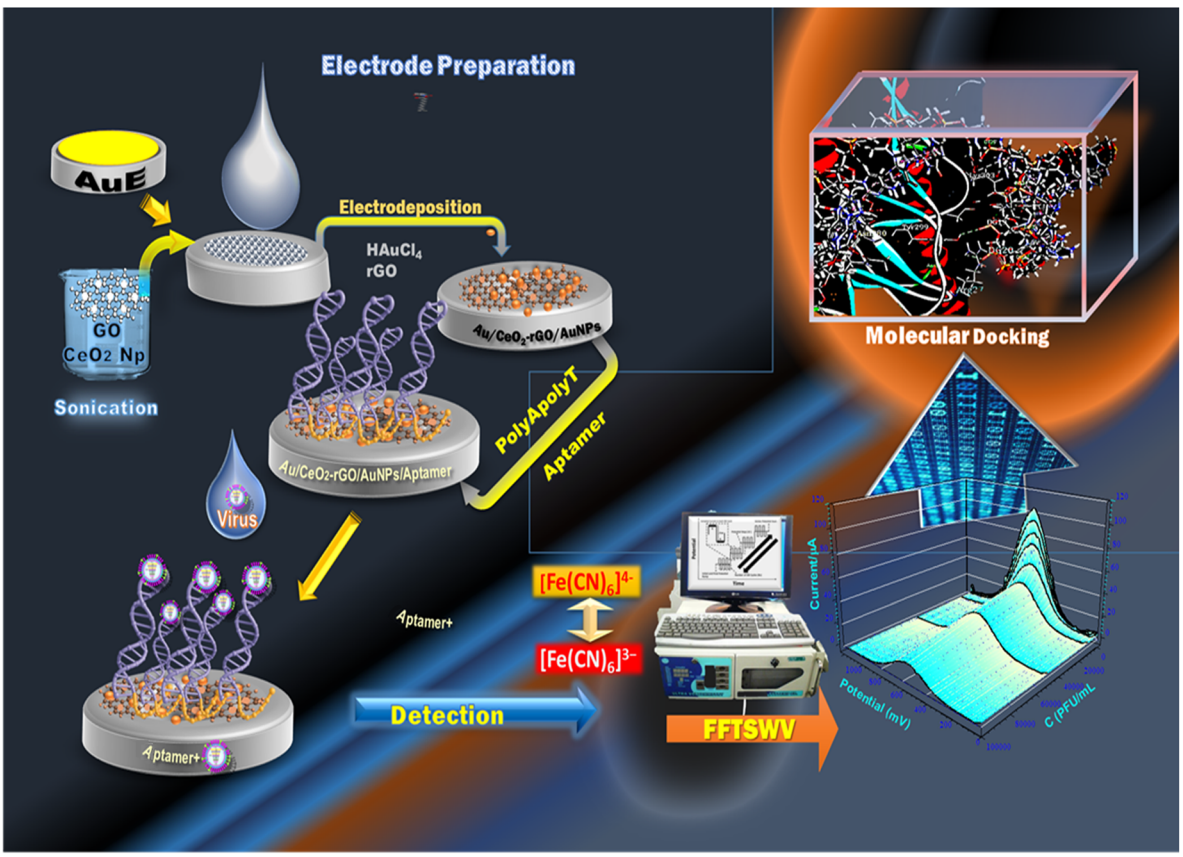

Scheme 1 Diagram presentation of preparation steps of aptamer and the generated response by potentiostat and FFTSWV and molecular docking view of calculation.

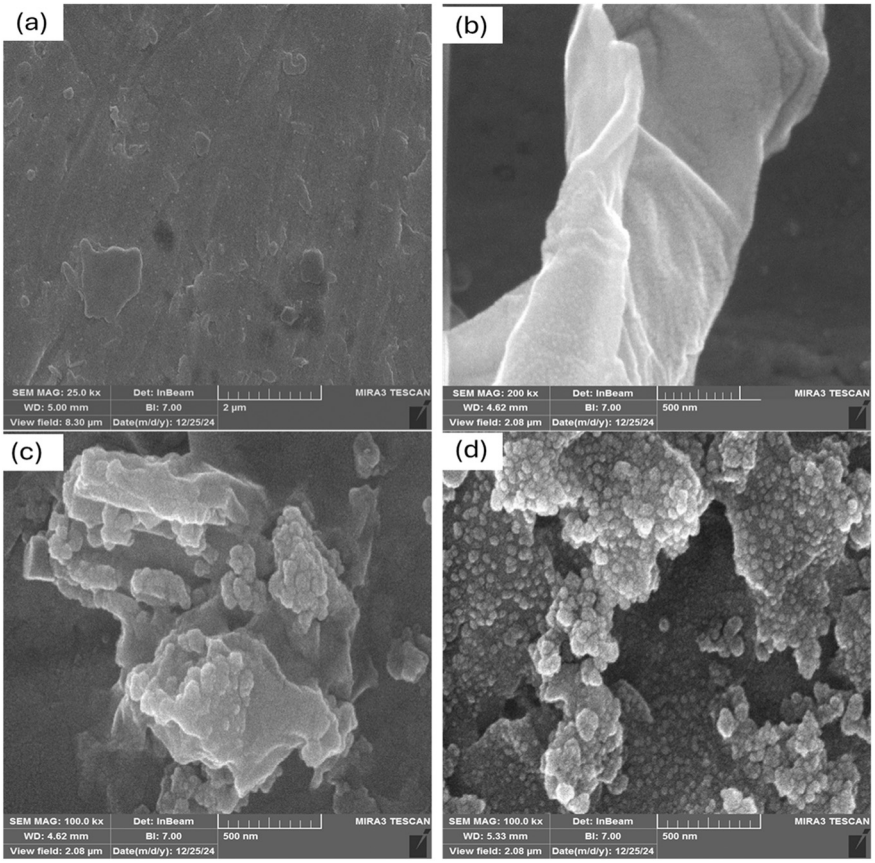

Fig. 1 FE-SEM images, EDX and maps of: (a) the bare AuE (Au), (b) the AuE/GO, (c) the AuE/nanoCeO$_2$–GO, (d) the AuE/nanoCeO$_2$-rGO/AuNPs.

of the interface. The pristine Au surface is smooth (Fig. 1a), whereas GO deposition yields the expected wrinkled, crumpled sheet morphology that increases accessible area and defect density for subsequent nucleation (Fig. 1b). Such corrugations are a well-established hallmark of GO films formed by exfoliation and drying.[33] Incorporation of spherical CeO_2 between GO layers produces a well-dispersed architecture (Fig. 1c) that introduces catalytically active sites and oxygen-vacancy-mediated pathways known to facilitate charge transfer at carbon/oxide interfaces.[34] Co-reduction of GO to rGO and Au^{3+} to AuNPs yields a compact Au/nanoCeO$_2$–rGO/AuNPs network with uniformly distributed nanoparticles (~27 nm; Fig. 1d). In analogous rGO/Au systems, AuNPs decrease interfacial impedance and accelerate $[Fe(CN)_6]^{3-/4-}$ kinetics, while rGO provides continuous, low-resistance pathways; combining these with CeO_2 typically enhances catalytic turnover and stability through synergistic coupling in the ternary composite.[35] Overall, the observed hierarchical structure aligns with prior CeO_2–rGO and AuNPs–rGO reports in which uniform nanoparticle dispersion within a crumpled carbon scaffold correlates with improved electron-transport channels and higher electroactive surface utilization, consistent with the performance trends discussed later.

Beyond morphological inspection, elemental analysis was employed to corroborate the successful incorporation and spatial distribution of all functional components within the multilayer electrode architecture. EDS spectra and corresponding elemental mapping for each stage of electrode modification, namely the bare gold electrode (Au), the Au/GO electrode, and the Au/nanoCeO$_2$–GO electrode, are provided in the SI, section S2 (Fig. S3–S5). Across these stages, the elemental signatures and spatial distributions are fully consistent with the corresponding FE-SEM micrographs, collectively verifying the sequential formation and structural integrity of each deposited layer. Representative elemental characterization of the final Au/nanoCeO$_2$–ErGO/AuNPs electrode is shown in Fig. 2, where Fig. 2(A) presents the EDS spectrum and semi-quantitative elemental composition, and Fig. 2(B) shows the corresponding elemental maps. The EDS spectrum exhibits distinct signals from C, O, Ce, and Au, confirming the successful integration of the ErGO scaffold, cerium oxide nanoparticles, and gold nanostructures in the final electrode architecture. Semi-quantitative analysis indicates carbon and oxygen contents of 21.11 wt% (47.04 at%) and 27.01 wt% (45.18 at%), respectively, consistent with an oxygen-rich ErGO/CeO_2 composite matrix. Cerium contributes 13.34 wt% (2.55 at%), while gold accounts for 38.54 wt% (5.24 at%), reflecting effective incorporation of AuNPs despite their lower atomic fraction relative to the lighter elements. Elemental mapping of the final modification step further demonstrates a homogeneous

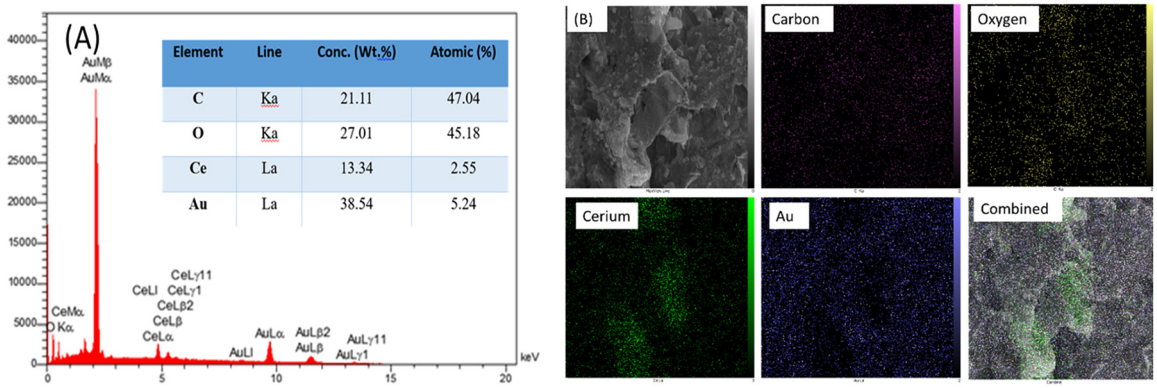

Fig. 2 (A) EDS spectrum and semi-quantitative elemental composition of the Au/nanoCeO$_2$–rGO/AuNPs electrode. (B) Corresponding elemental maps of C, O, Ce, and Au and their combined distribution, revealing uniform spatial integration of all components within the composite electrode.

spatial distribution of C, O, Ce, and Au across the electrode surface. The combined maps reveal strong spatial overlap between all elements, with no evidence of localized enrichment, phase segregation, or macroscopic agglomeration at the microscale. Notably, the Ce and Au signals closely follow the surface morphology observed in FE-SEM, indicating that both components are uniformly integrated within the ErGO framework rather than forming isolated domains. Taken together, the EDS spectra and elemental maps confirm the compositional uniformity and structural coherence of the final Au/nanoCeO$_2$–ErGO/AuNPs electrode, while the full set of supplementary EDS and mapping data demonstrates consistent agreement between elemental analysis and FE-SEM observations across all fabrication stages.

3.2 EC characterization of the aptasensor

Because both the immobilized aptamer and the target virus are electrochemically inactive within the applied potential window, the reversible $[Fe(CN)_6]^{3-/4-}$ redox couple was employed as an outer-sphere electrochemical probe to interrogate interfacial changes induced by successive surface modifications. Systematic variations in the probe's peak current and peak-to-peak separation (ΔE_p) reflect alterations in interfacial electron-transfer kinetics and probe accessibility arising from changes in surface structure and layer composition.[36,37] Fig. S6 presents the cyclic voltammograms recorded for the bare Au electrode, Au/nanoCeO$_2$–GO, Au/nanoCeO$_2$–rGO/AuNPs, and the aptamer-modified electrode before and after exposure to allantoic fluid and the H9N2 virus. The bare Au electrode exhibits well-defined redox peaks with relatively small ΔE_p, indicative of fast and reversible electron transfer at the conductive gold surface.[38] Following modification with the nanoCeO$_2$–GO layer, the redox current decreases and ΔE_p increases, consistent with partial surface blocking and reduced accessibility of the $[Fe(CN)_6]^{3-/4-}$ probe due to the oxygen-rich GO matrix. Subsequent co-electrodeposition of rGO and AuNPs leads to a pronounced enhancement of the redox current accompanied by a decrease in ΔE_p, reflecting restoration and improvement of interfacial electron-transfer kinetics through the formation of a conductive rGO network and uniformly distributed AuNPs. Quantitatively, the anodic peak current increases from approximately 34.1 μA at the bare Au electrode to 89.7 μA after formation of the nanoCeO$_2$–rGO/AuNP-modified interface, corresponding to an enhancement of about 163%, clearly demonstrating the significant contribution of the nanocomposite to electrochemical signal amplification. Immobilization of the ssDNA aptamer results in a decrease in peak current and an increase in ΔE_p, attributed to the introduction of a negatively charged, nonconductive biological layer that hinders probe diffusion and electron transfer. This effect arises from electrostatic repulsion between the negatively charged phosphate backbone of the aptamer and the $[Fe(CN)_6]^{3-/4-}$ redox probe, in addition to partial physical blocking of the electrode surface, which together reduce the accessibility of electroactive species to the interface. Exposure to allantoic fluid produces a modest additional suppression of the redox response, consistent with nonspecific surface coverage. These adsorbed biomolecules further limit diffusion pathways and increase interfacial resistance, although to a lesser extent compared to specific target binding. In contrast, incubation with the H9N2 virus causes a more pronounced reduction in current and further widening of ΔE_p, confirming the formation of the aptamer–virus complex and the associated increase in interfacial resistance. Notably, due to the relatively large size of H9N2 virions, their binding introduces significant steric hindrance, effectively blocking active sites and forming a physical barrier that prevents the redox probe from reaching the electrode surface for electron transfer. This leads to pronounced mass transport limitations and a substantial decrease in charge transfer efficiency. Collectively, these systematic changes in the $[Fe(CN)_6]^{3-/4-}$ response validate the stepwise construction of the sensing interface and its functional response to target binding.

To investigate the EC properties of the electrode surfaces, EIS experiments were conducted, which is a powerful technique that allows for the characterization of various electrochemical systems by providing insights into charge

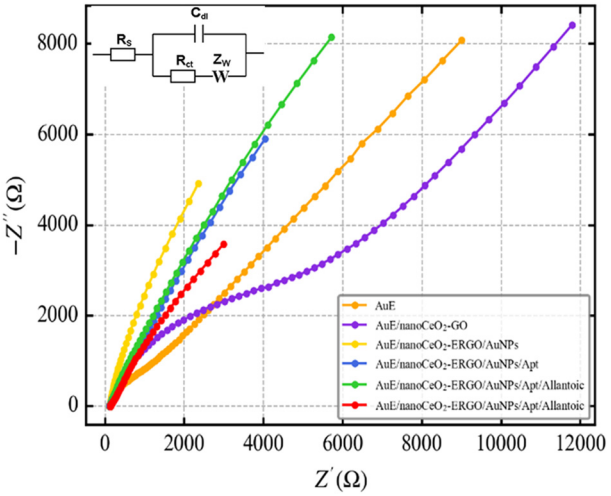

Fig. 3 Nyquist diagrams of bare Au, Au/nanoCeO$_2$–GO, Au/nanoCeO$_2$–rGO/AuNPs, Au/nanoCeO$_2$–rGO/AuNPs/Apt, Au/nanoCeO$_2$–rGO/AuNPs/Apt/allantoic, and Au/nanoCeO$_2$–rGO/AuNPs/Apt/allantoic/H9N2 in 0.1 M PBS solution (pH 7.5) containing 5 mmol L^{-1} $[Fe(CN)_6]^{3-/4-}$ and 250 mmol L^{-1} KCl, over the frequency range of 0.1 Hz to 1 MHz, with a DC potential of 0.2 V and an AC amplitude of 0.01 V. Inset: Equivalent circuit used to fit the obtained data.

transfer and diffusion processes. The Nyquist spectra in Fig. 3 presents the Nyquist plots obtained for the bare Au electrode and the successive surface-modified electrodes, including Au/nanoCeO$_2$–GO, Au/nanoCeO$_2$–rGO/AuNPs, and Au/nanoCeO$_2$–rGO/AuNPs/Apt. The impedance measurements were performed over a frequency range of 0.1 Hz to 1 MHz using a DC potential of 0.2 V and an AC perturbation of 10 mV in 0.1 M PBS (pH 7.5) containing 5 mmol L^{-1} $[Fe(CN)_6]^{3-/4-}$ and 250 mmol L^{-1} KCl. Across all electrode configurations, the spectra consist of a finite semicircular feature in the high-to-intermediate frequency region followed by an inclined low-frequency tail, indicative of heterogeneous interfacial kinetics and diffusion-limited transport at the electrode–electrolyte interface.[39] The bare Au electrode displays the smallest semicircle diameter, corresponding to minimal charge-transfer resistance and efficient electronic coupling between the outer-sphere $[Fe(CN)_6]^{3-/4-}$ redox couple and the metallic surface. Upon introduction of the nanoCeO$_2$–GO layer, the semicircle expands substantially, reflecting a pronounced increase in interfacial resistance. This behavior arises from partial surface coverage by oxygen-rich GO domains, reduced electronic conductivity, and electrostatic exclusion of the anionic redox probe, which collectively suppress interfacial electron-transfer kinetics. Formation of the Au/nanoCeO$_2$–ErGO/AuNPs composite leads to a marked contraction of the semicircular region accompanied by a more linear low-frequency impedance response. This evolution indicates restoration of charge-transfer efficiency and improved ion transport at the interface, consistent with the establishment of a conductive percolation network mediated by ErGO and AuNPs. The reduction in charge-transfer resistance despite increased structural complexity highlights the synergistic role of conductive nanophases in compensating for the insulating contributions of oxide and residual oxygen functionalities. Following immobilization of the aptamer layer, the impedance response exhibits an increased semicircle diameter, indicating elevated interfacial resistance due to the introduction of a non-conductive, negatively charged molecular overlayer. This modification imposes steric and electrostatic constraints that limit probe accessibility and attenuate electron exchange. Subsequent exposure to allantoic fluid produces only minor impedance changes, suggesting minimal nonspecific adsorption and preservation of the interfacial architecture. Upon incubation with the H9N2 virus, a further increase in charge-transfer resistance is observed, consistent with formation of the aptamer–virus complex and enhanced interfacial blocking by electrochemically inactive viral particles. The concurrent evolution of the low-frequency impedance response reflects increased diffusional constraints in the interfacial region. The monotonic increase in interfacial resistance upon specific target binding, together with the weak response to the matrix control, confirms that signal transduction is governed by selective modulation of interfacial impedance rather than bulk solution effects. The equivalent circuit, resulting from the curve fitting and analysis of the EIS curve $[R_s(C_{dl}[R_{ct}W])]$, is illustrated in Fig. 3 (inset), R_s = solution resistance, C_{dl} = capacitance of the double layer, R_{ct} = charge transfer resistance, and W represents Warburg impedance.

Overall, the systematic evolution of charge-transfer and diffusion-related impedance components across successive modification steps provides strong evidence that the sensing mechanism is controlled by regulation of interfacial electron-transfer pathways. The agreement between impedance-derived trends and voltammetric observations further supports impedance modulation as the dominant transduction mechanism of the developed aptasensor.

3.2.1 Optimization of analytical conditions. To ensure optimal performance of the aptasensor, a series of optimization studies were conducted step-by-step by using FFT-SWV. These parameters were classified into two groups: environmental (including AuNPs electrodeposition time, pH, concentration, and incubation time of the aptamer, as well as H9N2 virus immobilization time) and instrumental (*i.e.*, frequency and amplitude of the applied potential). The experiments were systematically conducted using a one-variable-at-a-time approach, where only a single parameter was altered in each run, while all other conditions remained constant.

3.2.2 Optimization of fabrication parameters. To maximize aptasensor performance, key fabrication parameters that govern interfacial conductivity and probe loading must be optimized, including the AuNP electrodeposition time, which directly controls nanoparticle coverage on the pre-modified gold electrode. Accordingly, the electrochemical response was evaluated for deposition times of 50–300 s (50 s increments). To quantify the analytical response, the peak current obtained in the absence of target (I_0) was compared with the current measured after incubation with H9N2 (I_c), and

the signal difference was defined as $\Delta I_p = I_0 - I_c$. This signal-off behavior reflects progressive interfacial blocking induced by formation of the aptamer–HA complex, which restricts electron transfer of the redox probe at the electrode surface. Because neither the aptamer nor the virus is intrinsically electroactive, the observed signal modulation arises exclusively from target-induced changes in interfacial accessibility and charge-transfer efficiency, rather than direct redox reactions of the analyte. As shown in Fig. 4A, the signal increased with deposition time and reached a maximum at 250 s, consistent with increased coverage of well-dispersed AuNPs that enhances electron transfer and increases the density of active sites for aptamer immobilization. At shorter times (<250 s), AuNP nucleation/growth is insufficient, yielding limited coverage and fewer attachment sites, which constrains signal enhancement. In contrast, longer deposition (>250 s) reduced the response, likely due to excessive growth and particle coalescence that densify the surface into a thicker, more continuous gold layer, thereby lowering the effective electroactive area, limiting probe accessibility, and restricting aptamer accessibility and conformational freedom. Consequently, aptamer–HA complex formation becomes less efficient, leading to decreased sensitivity at prolonged deposition times.[40,41]

Buffer pH plays a critical role in aptasensor performance by influencing the conformation, surface orientation, and binding affinity of the aptamer toward its target.[42,43] Therefore, the pH was systematically varied from 6.5 to 8.5. Deviations toward either acidic or alkaline conditions can disrupt the aptamer's three-dimensional structure through protonation or deprotonation of nucleobases, leading to reduced binding efficiency. In addition, non-neutral pH conditions may alter interfacial charge distribution and accelerate electrode or material degradation, further affecting electron transfer processes and signal stability.[44–46] As shown in Fig. 4B, the peak current increased with pH and reached a maximum at pH 7.5, indicating optimal aptamer–hemagglutinin (HA) interaction under near-neutral conditions. At lower pH, structural distortion of the aptamer reduces target recognition, while at higher pH, changes in surface charge and interfacial properties hinder effective binding and electron transfer.[47] Accordingly, pH 7.5 was selected as the optimal condition, providing a balance between aptamer structural stability, efficient target binding, and favorable electrochemical response.

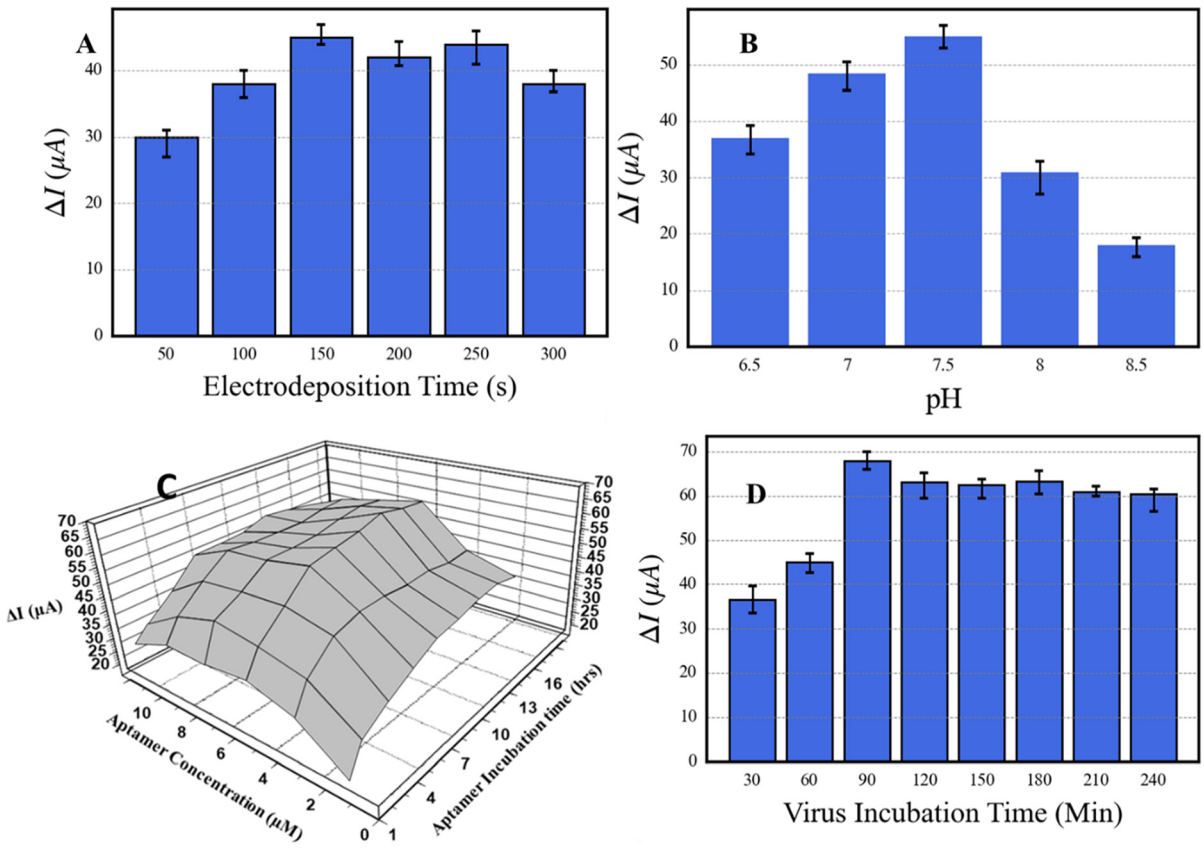

Fig. 4 The effects of (A) AuNPs electrodeposition time, (B) pH value, (C) aptamer concentration and incubation time, (D) virus incubation time, on the FFT-SWV response of the aptasensor. FFTSWV measurements were performed in 0.1 M KCl electrolyte PBS solution, pH 7.5 containing 5 mM $[Fe(CN)_6]^{3-}$, presence of 1.0×10^3 PFU mL^{-1} of H9N2 virus, in the potential range of 0–700 mV, frequency of 177 Hz, amplitude of 20 mV, and SW cycles 120.

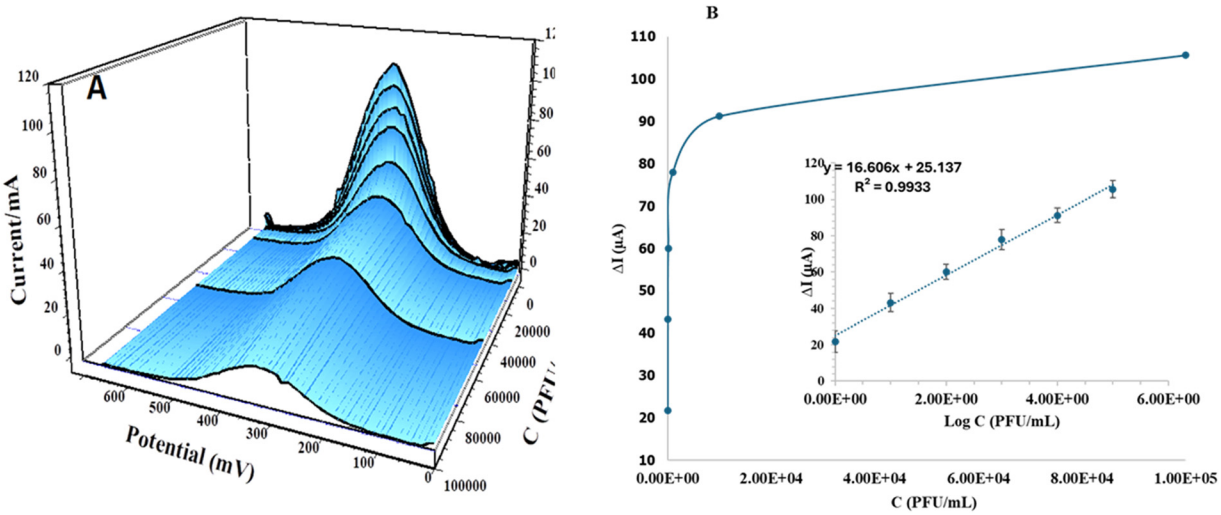

Fig. 5 (A) FFT-SW responses of 5 μM aptamer recorded at (A) Au/nanoCeO$_2$–rGO/AuNPs/Apt and after interaction with different concentrations of 1.0 × 10^1 to 1.0 × 10^5 (PFU mL^{-1}) of H9N2, (B) the baseline corrected signal (Δ*I*) of the aptasensor *vs.* the concentration range of 1.0 × 10^1 to 1.0 × 10^5 of H9N2; inset: the baseline corrected signal (Δ*I*) of the aptasensor *vs.* concentration logarithm 1.0 × 10^1 to 1.0 × 10^5 in the potential range of 0–700 mV, frequency of 177 Hz, amplitude of 20 mV in PBS pH 7.5 containing 5 mmol L^{-1} $[Fe(CN)_6]^{3-/4-}$ and 250 mmol L^{-1} KCl.

Accordingly, the electrochemical response was evaluated using aptamer concentrations of 1–10 μmol L^{-1} (serial dilutions) and incubation times of 1–16 h in the presence of 1.0 × 10^3 PFU mL^{-1} H9N2 at pH 7.5. As shown in Fig. 4C, increasing the aptamer concentration enhanced the response up to an optimum of 5 μmol L^{-1}, consistent with increased surface coverage and a higher density of accessible recognition sites for virus binding.[48] In contrast, concentrations above 5 μmol L^{-1} reduced the response, likely due to excessive surface packing that introduces electrostatic repulsion between DNA backbones and steric hindrance, which together limit target accessibility and impede efficient interfacial charge transfer.[49] At lower aptamer concentrations, incomplete coverage reduces available binding sites, resulting in a diminished electrochemical response.

In parallel, incubation time was optimized to ensure stable aptamer immobilization on the nanostructured surface. Increasing the immobilization period enhanced the response up to 8 h, consistent with sufficient time for aptamer adsorption, orientation, and stabilization into a well-organized recognition layer. Beyond 8 h, no meaningful signal improvement was observed, indicating surface saturation; extended incubation may also promote rearrangement/crowding without further performance gains. Accordingly, an aptamer concentration of 5 μmol L^{-1} and an immobilization time of 8 h were selected as the optimal conditions for subsequent experiments. The virus incubation time was then optimized by varying exposure from 30 to 240 min. As shown in Fig. 4D, the maximum electrochemical response was obtained at 90 min incubation in allantoic fluid. At longer times, the response decreased and then stabilized up to 240 min, likely due to saturation of surface-bound virus complexes that hinder diffusion of the redox probe to the electrode interface.

3.2.3 Optimization of EC parameters. The FFT-SWV parameters (frequency, amplitude, and number of cycles) were systematically optimized to balance faradaic response, capacitive effects, and kinetic limitations at the electrode interface (see section SI-4). The results demonstrate that both excessively high and low effective sweep rates lead to signal distortion, while optimal conditions maximize the faradaic contribution. Accordingly, 177 Hz, 20 mV, and N_{sw} = 120 were selected for subsequent analyses (see Fig. S7).

3.3 Analytical performance of the aptasensor

The analytical performance of the AuE/nanoCeO$_2$–rGO/AuNPs aptasensor for detection of the H9N2 influenza hemagglutinin (HA) antigen was systematically evaluated using Fast Fourier Transform square-wave voltammetry (FFT-SWV). Unlike conventional square-wave or differential pulse techniques that operate purely in the time domain, FFT-SWV enables transformation of the electrochemical signal into the frequency domain, allowing selective isolation of faradaic components while suppressing background capacitive contributions and low-frequency noise. This dual electrochemical–signal-processing approach is particularly advantageous for biosensing in complex biological matrices, where non-specific adsorption and baseline drift often limit sensitivity. The sensor response was recorded over a concentration range of 1.0 × 10^1 to 1.0 × 10^5 PFU mL^{-1} of H9N2 virus in PBS (pH 7.5), using the reversible $[Fe(CN)_6]^{3-/4-}$ redox couple as an outer-sphere electrochemical probe. Measurements were performed under optimized FFT-SWV conditions (frequency 177 Hz, amplitude 20 mV, N_{sw} = 120) within a potential window of 0–700 mV. For each concentration, the Faradaic peak current was extracted from the processed FFT-SWV response (Fig. S2) following digital

filtering, background subtraction, and drift correction. Importantly, identical signal-processing procedures were applied across all concentrations, ensuring consistency and minimizing operator-dependent bias (Fig. 5A).

3.3.1 Calibration curve. To investigate the quantitative relationship between the electrochemical response and target concentration, a calibration curve was constructed by incubating the aptasensor with H9N2 virus concentrations ranging from 1.0×10^1–1.0×10^5 PFU mL^{-1} and recording the corresponding FFT-SW voltammetric signals. As shown in Fig. 5B, the plot of ΔI_p *versus* C exhibits a well-defined linear relationship, indicating a strong logarithmic dependence of the sensor response on virus concentration across the investigated range. With increasing H9N2 concentration, the electrochemical signal progressively decreased. This signal-off behavior arises from the formation of an insulating layer of aptamer–virus complexes on the electrode surface, which restricts both electron transfer and mass transport of the $[Fe(CN)_6]^{3-/4-}$ redox probe. Specifically, due to the relatively large size of H9N2 virions, their binding to the surface creates a steric barrier that physically blocks the active electrode sites, preventing the redox probe from approaching the electrode interface for effective electron transfer. As a result, the diffusion of $[Fe(CN)_6]^{3-/4-}$ toward the electrode becomes increasingly hindered, leading to mass transport limitations. This combination of surface blocking and restricted ion accessibility significantly reduces the probability of charge transfer events at the interface, thereby decreasing the measured current. As the surface coverage by non-conductive viral particles increases, interfacial accessibility is reduced, leading to a corresponding attenuation of the FFT-SW peak current. Linear regression of the calibration data yielded the equation $\Delta I_p = 16.606 \log C + 25.137$ where ΔI_p is expressed in μA and C in PFU mL^{-1}, with a high correlation coefficient ($R^2 = 0.9933$), confirming excellent linearity and analytical reliability. The limit of detection (LOD), calculated using the $3\sigma/m$ ($n = 5$), was determined to be 0.249 PFU mL^{-1}, with a relative standard deviation (RSD) of 3.24%, demonstrating the high sensitivity and reproducibility of the proposed aptasensing platform.

3.3.2 Selectivity of the aptasensor. To evaluate the selectivity of the aptasensors, three AuE/nanoCeO$_2$–rGO/AuNPs/Apt sensors were exposed to 10 μL of H5N8 fluid and an influenza vaccine containing three different subtypes of Influenza A virus (H1N1, H3N2, and H5N8) as well as two subtypes of Influenza B viruses, all at a concentration of 1.0×10^3 PFU mL^{-1}. The signal intensity was recorded during these experiments. As shown in Fig. 6, the highest signal intensity (100%) was observed when the Au/nanoCeO$_2$–rGO/AuNPs aptasensor interacted with the H9-HA protein, indicating a strong affinity of the proposed aptasensor for the H9N2 virus. Following introduction to the influenza vaccine, a significant drop in signal intensity was noted for the two Influenza A viruses (10% for H1N1 and 8% for H3N2). This decrease was attributed to the distinct HA properties present on the surfaces of the viruses, which resulted in non-specific

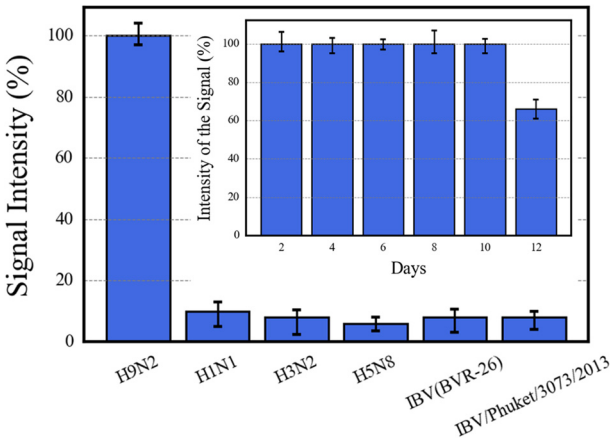

Fig. 6 The aptasensor relative responses after incubation with 10 μL a H5N8 fluid, and an influenza vaccine; containing 3 different subtypes of influenza A virus (H1H1, H3N2 and H85N8), and 2 subtypes of the influenza B viruses, and the inset, test of stability of the aptasensors under the mentioned condition in Fig. 4, preserved at 4 °C for 12 days.

interactions between the aptasensor and these subtypes. The signal intensity for the two Influenza B viruses present in the vaccine was also low (8%), reflecting the limited affinity of the immobilized aptamer for these viruses. This reduced affinity can be explained by the differing antigenic properties of the influenza B viruses compared to those of influenza A, leading to significant non-specific interactions between the aptasensor and the subtypes. Additionally, the aptasensor was exposed to the H5N8 subtype, which resulted in the lowest signal value recorded for this subtype (6%). Consequently, it was determined that the aptasensor exhibits considerable sensitivity towards the H9N2 virus. The relative standard deviation (RSD) of five replicate measurements was calculated to be 4.3%.

3.3.3 Repeatability and stability of the aptasensor. The stability and reproducibility of an AuE/nanoCeO$_2$–rGO/AuNPs/Apt are critical performance parameters for its practical application in H9N2 detection. To evaluate the stability of this aptasensor, multiple identical sensors were fabricated and maintained at 4 °C for 12 days, notably without the use of chemical preservatives, which is crucial for evaluating intrinsic stability, Fig. 7 Measurements were systematically performed every two days to monitor the sensor's response to H9N2 at a concentration of 1.0×10^3 PFU mL^{-1}.[50] Under constant experimental conditions, measurements were conducted every two days to measure the response to H9N2 at a concentration of 1.0×10^3 PFU mL^{-1}. The results indicated that the initial response remained stable at 100% after 10 days of fabrication. However, by day 12, a decrease in signal intensity to 78% of the original value was observed, which still reflects an acceptable level of stability for the fabricated aptasensor. The reproducibility of the aptasensor was evaluated by measuring the response (ΔI_p) using five similar modified electrodes, each incubated with 1.0×10^3 PFU mL^{-1} of H9N2 in a probe solution containing 5 mM $[Fe(CN)_6]^{3-/4-}$ and 0.1 M KCl. The relative

standard deviation (RSD) calculated for these electrodes was found to be 3.54%, indicating a high degree of consistency in the sensor's performance across multiple trials.

3.4 Molecular docking

To systematically compare the molecular recognition behavior of the candidate aptamers and rationalize their experimental binding performance, a multi-parameter docking analysis was conducted and evaluated alongside experimentally measured dissociation constants. Molecular docking simulations were performed for ten candidate DNA aptamers against the H9 hemagglutinin (HA) protein (PDB ID: 1JSD) to provide molecular-level insight into aptamer–target interactions and to support the experimental selection of an optimal recognition element for electrochemical sensing.[51,52] Docking calculations were carried out using the HDOCK platform, and for each aptamer, ten independent docking runs were performed under identical conditions to account for conformational sampling variability. The resulting mean docking score, mean confidence score, and mean ligand RMSD were extracted for each aptamer and are summarized together with the experimentally determined dissociation constants (K_d) in Table 1. Docking scores and confidence scores were used to assess relative interaction favorability and pose-ranking reliability within the docking framework, while ligand RMSD values were interpreted as indicators of pose dispersion across docking runs, reflecting the degree of convergence toward a consistent binding region on the protein surface rather than absolute structural stability.[53,54]

A comparative overview of these metrics is presented in Fig. 7. As shown, several aptamers, including A6, A21, and B25, exhibit more negative mean docking scores than B4, suggesting favorable interaction energies predicted by the docking algorithm. However, these aptamers also display substantially higher RMSD values, indicating broader pose dispersion and reduced localization of binding to a single region of the HA surface. This behavior suggests the presence of multiple competing binding orientations rather than a well-defined and reproducible recognition interface. In contrast, aptamer B4 demonstrates a balanced and favorable overall profile, combining a strong docking score (−273.47 kcal mol^{-1}), a high confidence score (0.9216), comparatively lower pose dispersion (mean RMSD = 70.53 Å), and the lowest experimentally measured dissociation constant (K_d = 7.38 ± 1.09 nM). The comparison in Table 1 and Fig. 7 highlights that docking score alone does not predict experimental binding affinity. For example, aptamer A6 achieves the most negative docking score (−283.49 kcal mol^{-1}) and the highest confidence score (0.934), yet its higher RMSD and weaker experimental affinity (K_d = 20.61 ± 7.55 nM) indicate less

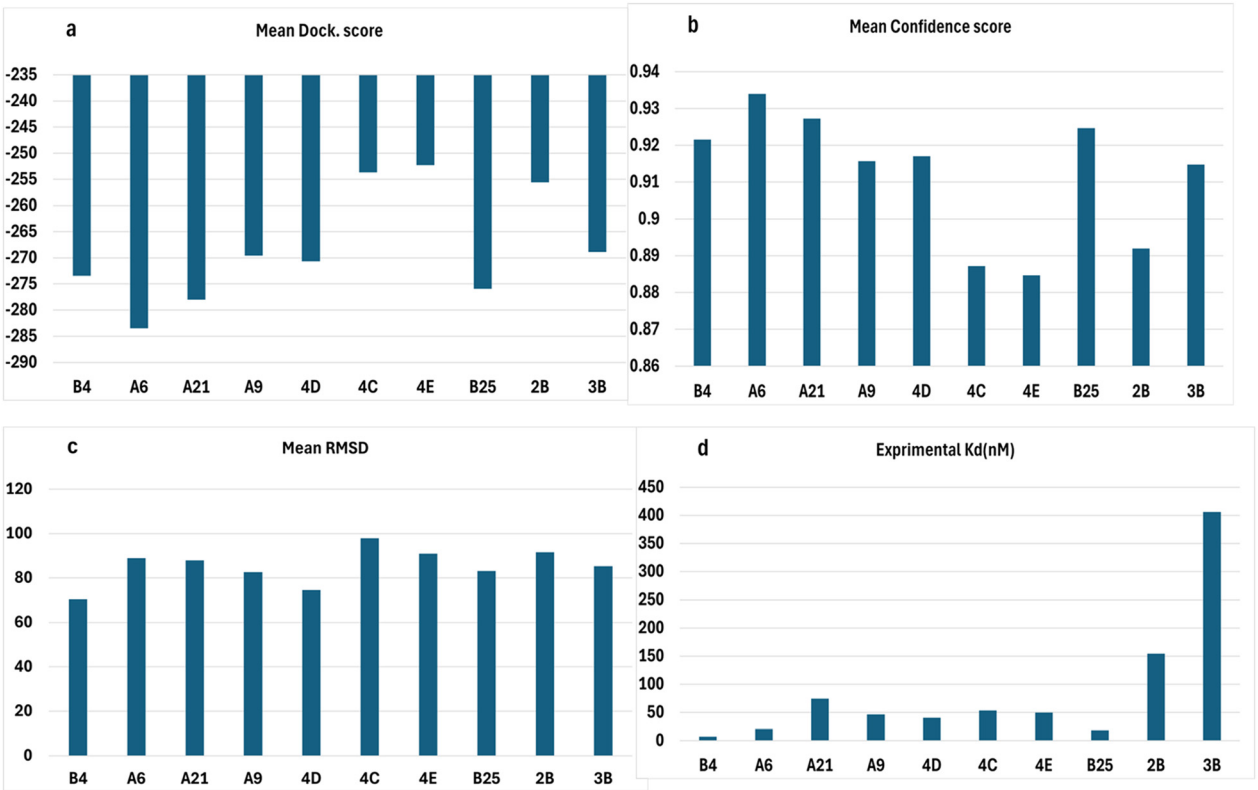

Fig. 7 Comparative analysis of 10 aptamers based on their (a) docking scores, (b) confidence scores, (c) ligand RMSD, and (d) K_d values. This multi-parameter assessment highlights the relative binding affinities and docking performance of each aptamer candidate, providing insight into their structural stability and interaction reliability.

Table 1 Aptamers with their corresponding dock score, confidential score, RMSD and K_d

Aptamer	Mean dock. score (kcal mol^{-1})	Mean Conf. score	Mean RMSD (Å)	K_d (nM)
B4	−273.47	0.9216	70.53	**7.38 ± 1.09**
A6	−283.49	0.934	88.9	20.61 ± 7.55
A21	−278.04	0.9273	87.93	74.27 ± 21.52
A9	−269.56	0.9157	82.58	46.23 ± 5.46
4D	−270.65	0.9170	74.52	40.67
4C	−253.69	0.8872	97.90	53.20
4E	−252.32	0.8847	90.9	49.46
B25	−275.95	0.9247	83.13	18.36 ± 2.10
2B	−255.61	0.892	91.58	154.64
3B	−268.89	0.9148	85.22	406.10

consistent and less effective binding under experimental conditions. Similarly, aptamers such as 2B and 3B exhibit relatively poor experimental affinities despite moderate docking metrics, reinforcing the importance of integrating computational and experimental data when selecting aptamer candidates.

To further elucidate the molecular basis of B4 recognition, detailed interaction analysis of the docked B4–HA complex is shown in Fig. 8. The electrostatic surface representation (Fig. 8A) reveals preferential association of aptamer B4 with positively charged, surface-exposed regions of the HA protein, supporting electrostatic complementarity with the negatively charged phosphate backbone of the DNA aptamer. Key residues located within the docked binding region include Lys303, Tyr299, Gly301, Thr281, and Thr282, which collectively contribute to stabilizing the aptamer–protein interface.[55] A close-up view of the docked complex (Fig. 8B) shows that several HA residues, including ARG276, TYR299, ASN280, and LYS303, participate in hydrogen bonding and electrostatic interactions with aptamer nucleotides such as DG19, DG20, and DC28. These interactions define a coherent and spatially focused binding interface. Hydrogen-bond analysis (Table S1) indicates that aptamer B4 forms 17 hydrogen bonds within optimal interaction distances (2.0–3.5 Å), distributed across 46 interacting residues, resulting in a dense and strategically positioned interaction network.[56]

Sequence-level analysis further indicates that nucleotides 18–31 of the aptamer sequence are predominantly involved in HA recognition (Fig. 8C), consistent with a 5′-end binding orientation. This binding mode aligns with the intended biosensor design, in which the 3′ terminus remains available for immobilization on the electrode surface. In contrast, other aptamers with comparable docking scores exhibit either reduced hydrogen-bond density, interactions with less conserved peripheral residues, or higher pose dispersion, which may account for their weaker experimental binding affinities.[57]

Overall, the molecular docking results provide mechanistic support for the experimental selection of aptamer B4. Rather than relying on a single computational metric, the combined evaluation of docking score trends, pose dispersion, electrostatic complementarity, interaction topology, binding orientation, and experimental affinity identifies B4 as the most suitable candidate for electrochemical biosensing. These molecular-level findings are consistent with the electrochemical results, in which formation of the aptamer–virus complex induces effective interfacial blocking and modulation of charge-transfer processes, thereby validating

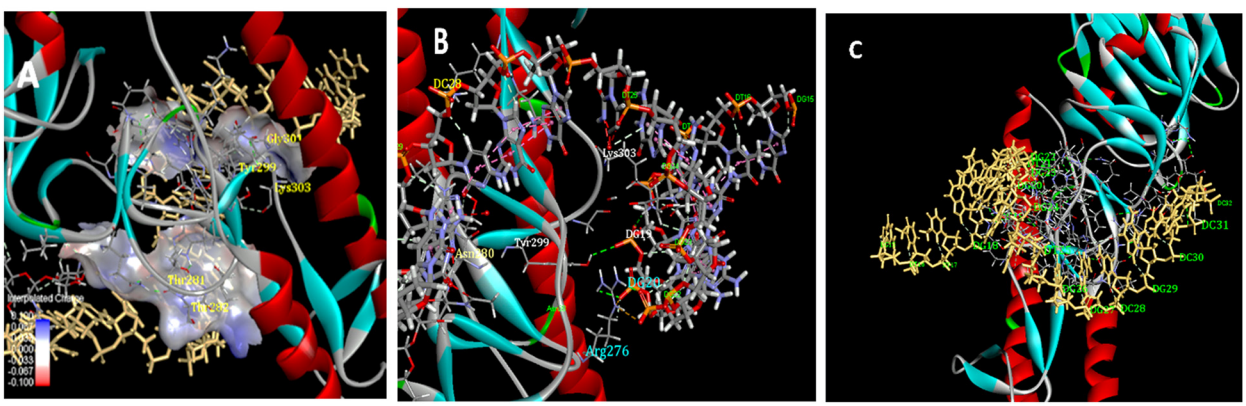

Fig. 8 (A) Electrostatic surface of the B4–protein complex. B4 binds to positively charged regions near Lys303, Tyr299, Gly301, Thr281, and Thr282, supporting stable electrostatic interactions. (B) Docked complex betsween the aptamer and the viral protein showing key interaction residues at the binding interface. Several critical protein residues, including ARG276, TYR299, ASN280, and LYS303, are engaged in hydrogen bonding and electrostatic interactions with aptamer nucleotides such as DG19, DG20, and DC28, (C) residues 18S–31S involved in the receptor–aptamer binding.

Table 2 Comparison of reported electrochemical biosensors developed for H9N2 influenza virus detection

Virus	Sensor platform	Detection method	LOD/linear range	Recognition element	Ref.
H9N2 AIV	Immunomagnetic separation + AuNP catalysis (SPCE)	Chronoamperometry	~16 HAU/8–128 HAU	Antibody (anti-M2)	1
H9N2 HA	Flexible CNT–PDMS paper immunosensor	DPV	54.0 pg mL^{-1}/ 100 pg mL^{-1}–100 ng mL^{-1}	Polyclonal antibody	15
H9N2 AIV	Pt–liposome + magnetic capture (SPCE)	Amperometry (collision)	18.1 fg mL^{-1}/ 25 fg mL^{-1}–25 ng mL^{-1}	Antibody (HRP-free catalytic labels)	12
H9N2 AIV	CeO_2–GO/PtNP nanocomposite immunosensor	Amperometry	0.43 pg mL^{-1}	Antibody	59
H1N1	$Ru(bpy)_3$@SiO_2 + magnetic separation	Electrochemiluminescence	3.54 μg mL^{-1}	H1 antibody	59
H9N2	Graphene–Au nanocomposite sensor	Amperometry	10^{-8} U mL^{-1}	Enzymatic	60
H5 AIV	Graphene oxide immunosensor	DPV	2^{-15} HA unit	Antibody	61
H7N9	DNA tetrahedral electrochemical biosensor	Amperometry	100 fM	DNA probe	62
H9N2 AIV	AuE/nanoCeO_2–rGO/AuNPs aptasensor	FFT-SWV	**0.249 PFU mL^{-1}**	DNA aptamer (B4), PolyA–PolyT	This study

the aptamer selection strategy. To contextualize the analytical performance and practical utility of the proposed aptasensor, we compared its key features with previously reported electrochemical platforms developed specifically for H9N2 detection (Table 2). Most existing systems employ antibody-based recognition combined with magnetic separation or catalytic amplification, which, despite reasonable sensitivity, require multi-step fabrication, conjugation steps, and rely on protein stability. For instance, sensors using Pt-loaded liposomes[12] or gold nanoparticle–enzyme hybrids[58] involve extended probe preparation and complex assembly, potentially limiting reproducibility and scalability. In contrast, the present platform integrates a label-free aptamer modified with a PolyA–PolyT tail for thiol-free, orientation-controlled immobilization onto a rGO–CeO_2–AuNP-modified gold electrode. This simplifies fabrication by eliminating chemical crosslinkers, enzymes, or secondary labels, while enhancing binding density and stability. Signal readout is performed using fast Fourier transform square-wave voltammetry (FFT-SWV), enabling frequency-domain extraction of Faradaic responses and suppression of background interference. The aptasensor achieved a limit of detection of 0.249 PFU mL^{-1}, which is lower than all previously reported electrochemical systems for H9N2, along with a broad linear range (1.0 ×10 to 1.0 ×10^5 PFU mL^{-1}). It demonstrated selectivity against non-target viral strains and maintained reliable performance in both phosphate-buffered saline and allantoic fluid, with 78% signal retention after 12 days at 4 °C without stabilizers. These findings position the proposed sensor as a sensitive, structurally simplified, and application-ready alternative to more complex immuno-based electrochemical platforms for early-stage H9N2 detection.

4. Conclusion

H9N2 avian influenza virus is an epidemiologically important yet under-monitored zoonotic pathogen, acting as a genetic reservoir for emerging influenza strains with pandemic potential. Despite this significance, electrochemical biosensing strategies for H9N2 remain limited, particularly those offering high sensitivity and robustness in complex biological environments. This work addresses this gap by presenting a label-free electrochemical aptasensor specifically designed for H9N2 detection and validated through combined experimental and molecular-level analyses. Notably, this work represents, to the best of our knowledge, the first biosensor implementation of the B4 anti-H9N2 hemagglutinin aptamer as a biorecognition element, translating its previously reported affinity into an analytical sensing platform. The AuE/nanoCeO_2–rGO/AuNPs sensing interface provides a conductive and structurally favorable platform for aptamer immobilization and efficient interfacial charge-transfer modulation upon target binding. A key innovation of this study is the implementation of fast Fourier transform square-wave voltammetry (FFT-SWV), which enables frequency-domain extraction of Faradaic signals while suppressing capacitive background and low-frequency noise. This signal-processing advantage significantly improves the signal-to-noise ratio, resulting in a low detection limit of 0.249 PFU mL^{-1}, low relative standard deviation, and a wide linear response range. The observed signal-off behavior originates from the formation of non-conductive aptamer–virus complexes that hinder electron transfer of the $[Fe(CN)_6]^{3-/4-}$ probe. Molecular docking analysis independently corroborated this mechanism, revealing a well-defined and electrostatically favorable interaction between the selected B4 aptamer and the H9 hemagglutinin protein. The consistency between computational interaction features and experimental binding affinity validates the aptamer selection strategy and supports the electrochemical response mechanism. Overall, this study demonstrates that combining rational nanointerface engineering with frequency-domain electrochemical signal processing offers a powerful and underexplored approach for ultrasensitive viral detection. The modular design and FFT-SWV readout make the platform readily adaptable to other

viral or protein targets, highlighting its potential for future electrochemical diagnostics and early-warning biosensing applications.

Conflicts of interest

The authors declare that they have no known competing financial interests or personal relationships that could have appeared to influence the work reported in this paper.

Data availability

The datasets generated and/or analyzed during the current study are available from the authors upon reasonable request.

Supplementary information (SI) is available. See DOI: https://doi.org/10.1039/d6sd00020g

Acknowledgements

We thank Tehran University for providing the necessary facilities and support.

References

1 M. Sayhi, *et al.*, Electrochemical detection of influenza virus H9N2 based on both immunomagnetic extraction and gold catalysis using an immobilization-free screen printed carbon microelectrode, *Biosens. Bioelectron.*, 2018, **107**, 170–177.
2 F. Pinotti, *et al.*, Modelling the transmission dynamics of H9N2 avian influenza viruses in a live bird market, *Nat. Commun.*, 2024, **15**(1), 3494.
3 M. Sagong, *et al.*, Current situation and control strategies of H9N2 avian influenza in South Korea, *J. Vet. Sci.*, 2022, **24**(1), e5.
4 J. Hou, *et al.*, Rapid and reliable ultrasensitive detection of pathogenic H9N2 viruses through virus-binding phage nanofibers decorated with gold nanoparticles, *Biosens. Bioelectron.*, 2023, **237**, 115423.
5 Z. Hu, *et al.*, Impact of inactivated vaccine on transmission and evolution of H9N2 avian influenza virus in chickens, *npj Vaccines*, 2025, **10**(1), 67.
6 W. Song and K. Qin, Human-infecting influenza A(H9N2) virus: A forgotten potential pandemic strain?, *Zoonoses Public Health*, 2020, **67**(3), 203–212.
7 S. Azeem and K.-J. Yoon, Diagnostic Assays for Avian Influenza Virus Surveillance and Monitoring in Poultry, *Viruses*, 2025, **17**(2), 228.
8 K. Dziąbowska, E. Czaczyk and D. Nidzworski, Detection methods of human and animal influenza virus—current trends, *Biosensors*, 2018, **8**(4), 94.
9 F. Mollarasouli, *et al.*, Nanomaterials-based immunosensors for avian influenza virus detection, *Talanta*, 2024, **279**, 126591.
10 X. Fu, *et al.*, Advances in detection techniques for the H5N1 avian influenza virus, *Int. J. Mol. Sci.*, 2023, **24**(24), 17157.
11 H. O. Tabrizi, *et al.*, A low-cost handheld reconfigurable impedimetric readout system for diagnostics of viral infections, *IEEE Trans. Instrum. Meas.*, 2023, **72**, 1–8.
12 J. Liu, *et al.*, A general controllable release amplification strategy of liposomes for single-particle collision electrochemical biosensing, *Biosens. Bioelectron.*, 2022, **207**, 114182.
13 C. H. Zhou, *et al.*, Electrochemical magnetoimmunosensing approach for the sensitive detection of H9N2 avian influenza virus particles, *Chem. – Asian J.*, 2013, **8**(9), 2220–2226.
14 C.-H. Zhou, *et al.*, A magnetic bead-based bienzymatic electrochemical immunosensor for determination of H9N2 avian influenza virus, *Electrochem. Commun.*, 2013, **31**, 129–132.
15 D. Lee, J. Bhardwaj and J. Jang, based electrochemical immunosensor for label-free detection of multiple avian influenza virus antigens using flexible screen-printed carbon nanotube-polydimethylsiloxane electrodes, *Sci. Rep.*, 2022, **12**(1), 2311.
16 B. Sequeira-Antunes and H. A. Ferreira, Nucleic acid aptamer-based biosensors: a review, *Biomedicines*, 2023, **11**(12), 3201.
17 R. Salahandish, *et al.*, Bi-ECDAQ: An electrochemical dual-immuno-biosensor accompanied by a customized bi-potentiostat for clinical detection of SARS-CoV-2 Nucleocapsid proteins, *Biosens. Bioelectron.*, 2022, **203**, 114018.
18 K. Mpofu, *et al.*, Aptamers and antibodies in optical biosensing, *Discov. Chem.*, 2025, **2**(1), 23.
19 S. Arshavsky-Graham, *et al.*, Aptamers vs. antibodies as capture probes in optical porous silicon biosensors, *Analyst*, 2020, **145**(14), 4991–5003.
20 Y. Zhang, *et al.*, Two DNA aptamers against avian influenza H9N2 virus prevent viral infection in cells, *PLoS One*, 2015, **10**(3), e0123060.
21 F. Charbgoo, M. Ramezani and M. Darroudi, Bio-sensing applications of cerium oxide nanoparticles: advantages and disadvantages, *Biosens. Bioelectron.*, 2017, **96**, 33–43.
22 S. Jarić, *et al.*, Direct electrochemical reduction of graphene oxide thin film for aptamer-based selective and highly sensitive detection of Matrix metalloproteinase 2, *Talanta*, 2024, **274**, 126079.
23 N. Heidari, *et al.*, Fast Fourier Transform-Based Activation and Monitoring of Micro-Supercapacitors: Enabling Energy-Autonomous Actuators. in *Actuators*, MDPI, 2025.
24 A. Opdahl, *et al.*, Independent control of grafting density and conformation of single-stranded DNA brushes, *Proc. Natl. Acad. Sci. U. S. A.*, 2007, **104**(1), 9–14.
25 X. Wang, *et al.*, Rapid Construction of Thiolated DNA-AuNP Conjugates via PolyA Blocking for Precise Control of Surface Functionalization, *Langmuir*, 2026, 3080–3088.
26 Z. Shang, *et al.*, Construction and bioanalytical applications of poly-adenine-mediated gold nanoparticle-

based spherical nucleic acids, *Anal. Methods*, 2023, **15**(42), 5564–5576.
27 W. Lu, *et al.*, Quantitative investigation of the poly-adenine DNA dissociation from the surface of gold nanoparticles, *Sci. Rep.*, 2015, **5**(1), 10158.
28 Sanofi, *VaxigripTetra® – Summary of Product Characteristics*, retrieved from, 2023, [cited 2025 July 17], available from: https://www.sanofi.com/en/our-products/vaxigriptetra.
29 X. Nie, *et al.*, Sensitive and selective determination of tryptophan using a glassy carbon electrode modified with nano-CeO2/reduced graphene oxide composite, *Microchem. J.*, 2020, **159**, 105367.
30 M. Shen and X. Kan, Aptamer and molecularly imprinted polymer: Synergistic recognition and sensing of dopamine, *Electrochim. Acta*, 2021, **367**, 137433.
31 J. Bolduc, *et al.*, Peroxiredoxins wear many hats: Factors that fashion their peroxide sensing personalities, *Redox Biol.*, 2021, **42**, 101959.
32 D. Kozakov, *et al.*, The ClusPro web server for protein-protein docking, *Nat. Protoc.*, 2017, **12**(2), 255–278.
33 M. P. Weir, *et al.*, Extrinsic wrinkling and single exfoliated sheets of graphene oxide in polymer composites, *Chem. Mater.*, 2016, **28**(6), 1698–1704.
34 A. Murali, *et al.*, Synthesis of CeO2/reduced graphene oxide nanocomposite for electrochemical determination of ascorbic acid and dopamine and for photocatalytic applications, *Mater. Today Chem.*, 2019, **12**, 222–232.
35 F. Kong, *et al.*, Reduced graphene oxide and gold nanoparticles-modified electrochemical aptasensor for highly sensitive detection of doxorubicin, *Nanomaterials*, 2023, **13**(7), 1223.
36 E. Laviron, General expression of the linear potential sweep voltammogram in the case of diffusionless electrochemical systems, *J. Electroanal. Chem. Interfacial Electrochem.*, 1979, **101**(1), 19–28.
37 N. Heidari, *et al.*, A novel label-free immunosensor for detection of VEGF using FFT admittance voltammetry, *Bioelectrochemistry*, 2025, **165**, 108948.
38 M. Karimzade, *et al.*, The rGO@ AuNPs modified label-free electrochemical immunosensor to sensitive detection of CP-BNYVV protein of Rhizomania disease agent in sugar beet, *Plant Methods*, 2024, **20**(1), 181.
39 H. Zhang, *et al.*, Electrochemical impedance spectroscopy-based biosensors for label-free detection of pathogens, *Biosensors*, 2025, **15**(7), 443.
40 X. Dai, *et al.*, Electroanalysis using macro-, micro-, and nanochemical architectures on electrode surfaces. Bulk surface modification of glassy carbon microspheres with gold nanoparticles and their electrical wiring using carbon nanotubes, *Anal. Chem.*, 2006, **78**(17), 6102–6108.
41 N. D. Zakaria, *et al.*, Effect of supporting background electrolytes on the nanostructure morphologies and electrochemical behaviors of electrodeposited gold nanoparticles on glassy carbon electrode surfaces, *ACS Omega*, 2021, **6**(38), 24419–24431.
42 L. Li, *et al.*, Modulating aptamer specificity with pH-responsive DNA bonds, *J. Am. Chem. Soc.*, 2018, **140**(41), 13335–13339.
43 K. Jakab, *et al.*, Comparative analysis of pH and target-induced conformational changes of an oxytetracycline aptamer in solution phase and surface-immobilized form, *Biomolecules*, 2023, **13**(9), 1363.
44 K. M. Koo, *et al.*, DNA–bare gold affinity interactions: mechanism and applications in biosensing, *Anal. Methods*, 2015, **7**(17), 7042–7054.
45 J. Yan, *et al.*, Sensitive and rapid detection of influenza A virus for disease surveillance using dual-probe electrochemical biosensor, *Bioelectrochemistry*, 2023, **153**, 108497.
46 C. Singhal, *et al.*, *Label-Free Electrochemical Nano-Sensors for Detection of Acinetobacter Baumannii: Unveiling the Kinetic Behaviour of Reduced Graphene Oxide v/s Graphene Oxide*, 2023.
47 S. Li, *et al.*, A pH-independent electrochemical aptamer-based biosensor supports quantitative, real-time measurement in vivo, *Chem. Sci.*, 2022, **13**(30), 8813–8820.
48 S. Chauhan and J. W. Lee, Development of a Femtosensitive Electrochemical Aptasensor for Tuberculosis Ag85B Detection, *Anal. Chem.*, 2025, **97**(29), 15798–15807.
49 J. Upan, *et al.*, A simple label-free electrochemical sensor for sensitive detection of alpha-fetoprotein based on specific aptamer immobilized platinum nanoparticles/carboxylated-graphene oxide, *Sci. Rep.*, 2021, **11**(1), 13969.
50 X. Peng, *et al.*, Fluorescent-magnetic-catalytic nanospheres for dual-modality detection of H9N2 avian influenza virus, *ACS Appl. Mater. Interfaces*, 2019, **11**(44), 41148–41156.
51 Y. Yan, *et al.*, HDOCK: a web server for protein–protein and protein–DNA/RNA docking based on a hybrid strategy, *Nucleic Acids Res.*, 2017, **45**(W1), W365–W373.
52 Y. Zhang, *et al.*, Review of the applications of deep learning in bioinformatics, *Curr. Bioinf.*, 2020, **15**(8), 898–911.
53 K. E. Hevener, *et al.*, Validation of molecular docking programs for virtual screening against dihydropteroate synthase, *J. Chem. Inf. Model.*, 2009, **49**(2), 444–460.
54 L. G. Ferreira, *et al.*, Molecular docking and structure-based drug design strategies, *Molecules*, 2015, **20**(7), 13384–13421.
55 J.-F. Xiang, L. Yang and L.-L. Chen, The long noncoding RNA regulation at the MYC locus, *Curr. Opin. Genet. Dev.*, 2015, **33**, 41–48.
56 S. Song, *et al.*, Aptamer-based biosensors, *TrAC, Trends Anal. Chem.*, 2008, **27**(2), 108–117.
57 A. A. Lubin and K. W. Plaxco, Folding-based electrochemical biosensors: the case for responsive nucleic acid architectures, *Acc. Chem. Res.*, 2010, **43**(4), 496–505.
58 H. R. S. Lima, *et al.*, Electrochemical sensors and biosensors for the analysis of antineoplastic drugs, *Biosens. Bioelectron.*, 2018, **108**, 27–37.
59 Y. T. Büyüksünetçi and Ü. Anık, Electro-nano diagnostic platform based on antibody–antigen interaction: an

electrochemical immunosensor for influenza A virus detection, *Biosensors*, 2023, **13**(2), 176.
60 Ü. Anik, *et al.*, Towards the electrochemical diagnostic of influenza virus: Development of a graphene–Au hybrid nanocomposite modified influenza virus biosensor based on neuraminidase activity, *Analyst*, 2018, **143**(1), 150–156.
61 Z. Xie, *et al.*, Ultrasensitive electrochemical immunoassay for avian influenza subtype H5 using nanocomposite, *PLoS One*, 2014, **9**(4), e94685.
62 S. Dong, *et al.*, Electrochemical DNA biosensor based on a tetrahedral nanostructure probe for the detection of avian influenza A(H7N9) virus, *ACS Appl. Mater. Interfaces*, 2015, **7**(16), 8834–8842.